Active galactic nuclei winds as the origin of the H$_2$ emission excess in nearby galaxies

Rogemar A. Riffel [1,2]★ Nadia L. Zakamska [1] and Rogério Riffel [3]

[1]*Department of Physics & Astronomy, Johns Hopkins University, Bloomberg Center, 3400 N. Charles St, Baltimore, MD 21218, USA*
[2]*Departamento de Física, Centro de Ciências Exatas e Naturais (CCNE), Universidade Federal de Santa Maria, Santa Maria 97105-900, RS, Brazil*
[3]*Instituto de Física (IF), Universidade Federal do Rio Grande do Sul, CP 15051, Porto Alegre 91501-970, RS, Brazil*

ABSTRACT

In most galaxies, the fluxes of rotational H$_2$ lines strongly correlate with star formation diagnostics [such as polycyclic aromatic hydrocarbons (PAHs)], suggesting that H$_2$ emission from warm molecular gas is a minor by-product of star formation. We analyse the optical properties of a sample of 309 nearby galaxies derived from a parent sample of 2015 objects observed with the *Spitzer Space Telescope*. We find a correlation between the [O I]$\lambda6300$ emission-line flux and kinematics and the H$_2$ S(3) 9.665 μm/PAH 11.3 μm. The [O I]$\lambda6300$ kinematics in active galactic nuclei (AGNs) cannot be explained only by gas motions due to the gravitational potential of their host galaxies, suggesting that AGN-driven outflows are important to the observed kinematics. While H$_2$ excess also correlates with the fluxes and kinematics of ionized gas (probed by [O III]), the correlation with [O I] is much stronger, suggesting that H$_2$ and [O I] emissions probe the same phase or tightly coupled phases of the wind. We conclude that the excess of H$_2$ emission seen in AGNs is produced by shocks due to AGN-driven outflows and in the same clouds that produce the [O I] emission. Our results provide an indirect detection of neutral and molecular winds and suggest a new way to select galaxies that likely host molecular outflows. Further ground- and space-based spatially resolved observations of different phases of the molecular gas (cold, warm, and hot) are necessary to test our new selection method.

Key words: galaxies: active – galaxies: ISM – galaxies: kinematics and dynamics – galaxies: nuclei.

1 INTRODUCTION

Identifying and characterizing the processes that transform galaxies from star forming to quiescent is a fundamental goal of extragalactic astronomy (Conselice 2014; Hatfield & Jarvis 2017; Kim et al. 2018; Liu et al. 2018). Some of the critical transformation mechanisms include galactic-scale feedback due to active galactic nuclei (AGNs) or star formation. This feedback is now thought to be extremely important for galaxies of all mass scales (Cattaneo et al. 2009; Alexander & Hickox 2012; Fabian 2012; Harrison 2017). Galactic ionized gas outflows driven by AGNs (Liu et al. 2013; Carniani et al. 2015; Fischer et al. 2017) or star formation (Arribas et al. 2014; Gallagher et al. 2019) have been mapped in the last decade, leading to major improvements in understanding galactic winds. However, what happens to the molecular gas is much less clear. This component is of significant interest for understanding the impact of molecular outflows on star formation.

Studying cold ($T \lesssim 100$ K), warm ($T \sim$ a few hundred K), and hot ($T \gtrsim 1000$ K) phases of molecular gas is essential for understanding the origin and role of galactic molecular outflows. Studies of the inner kpc of nearby galaxies, using near-infrared (near-IR) integral field spectroscopy assisted by adaptive optics systems on 8–10 m class telescopes, have shown that hot molecular gas outflows are very scarce (Davies et al. 2014; Riffel, Storchi-Bergmann & Riffel 2015; May et al. 2018). Usually, the hot H$_2$ emission arises from the circumnuclear rotationally supported gas disc, sometimes showing streaming motions towards the nucleus (Riffel et al. 2008; Müller Sánchez et al. 2009; Riffel, Storchi-Bergmann & Winge 2013; Mazzalay et al. 2014; Durré & Mould 2019; Schönell et al. 2019).

Ultraluminous infrared galaxies (ULIRGs) seem to have an excess of hot molecular gas emission relative to that expected from their star formation rates (SFRs; Zakamska 2010), possibly due to shock heating by supernova- or AGN-driven outflows (Hill & Zakamska 2014; Imanishi, Nakanishi & Izumi 2018, 2019). Indeed, recent near-IR integral field spectroscopy reveals the presence of hot molecular gas outflows (Emonts et al. 2017) in three of the four observed ULIRGs. Cold molecular gas outflows are also commonly

Table 1. The sub-samples.

Name	No. of galaxies in Lambrides et al. ([2018](#))	No. of matches in SDSS	Comments
Sample Y	485	115	H_2 S(3) 9.665 µm and PAH 11.3 µm emission detected
Sample N	1503	193	H_2 S(3) 9.665 µm emission not detected
Other	27	1	H_2 S(3) detected, PAH not detected

observed in powerful AGNs (Feruglio et al. [2010](#); Fiore et al. [2017](#)). In nearby ULIRGs and AGN host galaxies, cold molecular outflows have been detected using *Herschel* spectra in the far-IR lines of OH (e.g. Fischer et al. [2010](#); Veilleux et al. [2013](#); González-Alfonso et al. [2014](#), [2017](#)) and spatially resolved with Atacama Large Millimeter Array (ALMA) observations of CO lines (e.g. Combes et al. [2013](#); García-Burillo et al. [2014](#); Morganti et al. [2015](#); Pereira-Santaella et al. [2018](#); Alonso-Herrero et al. [2019](#); Husemann et al. [2019](#); Ramakrishnan et al. [2019](#)). These studies reveal outflows with velocities ranging from few tens to over 1000 km s^{-1}, mass outflow rates of up to $10^3 \text{ M}_\odot \text{ yr}^{-1}$, and kinetic power as high as $10^{44} \text{ erg s}^{-1}$. Accelerating dense molecular gas to high enough velocities that they would escape the galaxy is extremely difficult, so modern theoretical work suggests that molecules may be formed within the outflow and may display excitation characteristics of shock heating (Richings & Faucher-Gière [2018a](#),[b](#)).

Understanding the acceleration and the emission mechanisms of molecular outflows – the critical ingredient in rapid star formation quenching – remains a major unsolved problem in galaxy formation. A recent study by Lambrides et al. ([2018](#)) provides an important new tool for understanding warm (a few hundred K) molecular gas emission in nearby galaxies. They analyse 2015 mid-IR spectra of galaxies observed with the *Spitzer Space Telescope* and provide fluxes of all emission features. Furthermore, they measure the excitation temperature of the H_2 S(5) and H_2 S(7) pure rotational transitions using stacked spectra of AGN-dominated and non-AGN-dominated sources. They find that the H_2 fluxes are higher in AGNs than in star-forming galaxies and the excitation temperature on AGN-dominated galaxies is $\sim$200 K larger, indicating that the AGNs play an important role in the H_2 emission. However, due to the low resolution of the *Spitzer* spectra, there is currently no available information on the H_2 kinematics, necessary to investigate whether the H_2 emission arises from shock-heated gas or whether it is due to local heating of the gas by AGNs or stellar radiation field.

In this paper, we cross-match the sample used by Lambrides et al. ([2018](#)) with the Sloan Digital Sky Survey (SDSS; Aguado et al. [2019](#)) spectroscopic data base in order to investigate the origin of the warm molecular hydrogen emission. This paper is organized as follows. Section 2 presents and characterizes the sample, and describes the data compilation and measurement procedure. In Section 3, we present our results, which are discussed in Section 4 and summarized in Section 5.

We use an $h = 0.7$, $\Omega_m = 0.3$, and $\Omega_\Lambda = 0.7$ cosmology. The wavelengths of the emission features in the IR are given in vacuum. The wavelengths of emission lines in the optical are given in the air (e.g. [O III]λ5007) following a long-standing tradition, even though the SDSS spectroscopic data base uses vacuum wavelengths. To test whether two distributions are statistically consistent (i.e. whether they are drawn from the same underlying distribution), we use the Kolmogorov–Smirnov test and report the probability of the null hypothesis P_{KS} that the two samples are consistent. A small value of P_{KS} implies a statistically significant difference in the distributions.

To test whether two parameters are correlated, we use the Pearson test to compute the P_{rank} value. A small value of P_{rank} implies a statistically significant correlation between the parameters and we consider that there is a correlation if $P_{rank} < 0.05$.

2 DATA AND MEASUREMENTS

2.1 The parent sample

Lambrides et al. ([2018](#)) analysed the molecular gas properties of a sample of 2015 galaxies ($0.002 < z < 3.0$) using mid-IR spectra obtained with the *Spitzer Space Telescope*. Their sample includes all objects observed as part of programmes containing at least one of the following keywords in their abstracts: AGN, radio galaxy, QSO, quasar, starburst galaxy, or ULIRG/LIRG, using the Infrared Spectrograph in the low-resolution modules (SL and LL), and they have excluded spectra with detection levels $<3\sigma$. Each module is divided into two spectroscopic orders: SL1 (7.46 µm $< \lambda <$ 14.29 µm), SL2 (5.13 µm $< \lambda <$ 14.29 µm), LL1 (19.91 µm $< \lambda <$ 39.90 µm), and LL2 (13.90 µm $< \lambda <$ 21.27 µm).

In this work, we cross-match the sample used by Lambrides et al. ([2018](#)) with the SDSS spectroscopic data base (Gunn et al. [2006](#); Blanton et al. [2017](#)). The SDSS spectra cover the range 3600–10300 Å at a resolving power $R \sim 2000$ and are part of the 15th Data Release (DR15) of the SDSS project (Aguado et al. [2019](#)). We use the SDSS Query/CasJobs platform to search for optical spectra of each object of the Lambrides sample. We include only objects photometrically identified as 'galaxy' and located closer than 0.1 arcmin from the *Spitzer* coordinates. We find that 309 galaxies from the sample of Lambrides et al. ([2018](#)) have spectra available in the DR15 of SDSS.

We divide the parent *Spitzer* sample into two sub-samples:

(i) Sample Y contains all objects with the H_2 S(3) 9.665 µm and polycyclic aromatic hydrocarbon (PAH) 11.3 µm emission lines detected. These are the most commonly detected H_2 and star formation diagnostics in the *Spitzer* data set. This sample contains 485 galaxies, with 115 matching the SDSS data base.

(ii) Sample N includes 1503 galaxies for which the H_2 S(3) 9.665 µm line was not detected in the *Spitzer* spectra. Spectra for 193 galaxies are available in the SDSS DR15.

In addition, for 27 objects the H_2 S(3) 9.665 µm line was detected, but with no detection of PAH 11.3 µm emission lines. Only one galaxy is in the SDSS data base. Table [1](#) lists the number of galaxies of each sub-sample as well as the number of objects with SDSS data available. In Fig. [1](#), we present examples of the typical SDSS spectra.

The flux limits of the *Spitzer* data may introduce biases in the H_2/PAH line ratios in each sample compared to a volume-limited sample of galaxies. However, the key scientific results of our paper focus on the objects in sample Y with the strongest H_2 emission, which are the least affected by the biases, and therefore our main results are not affected.
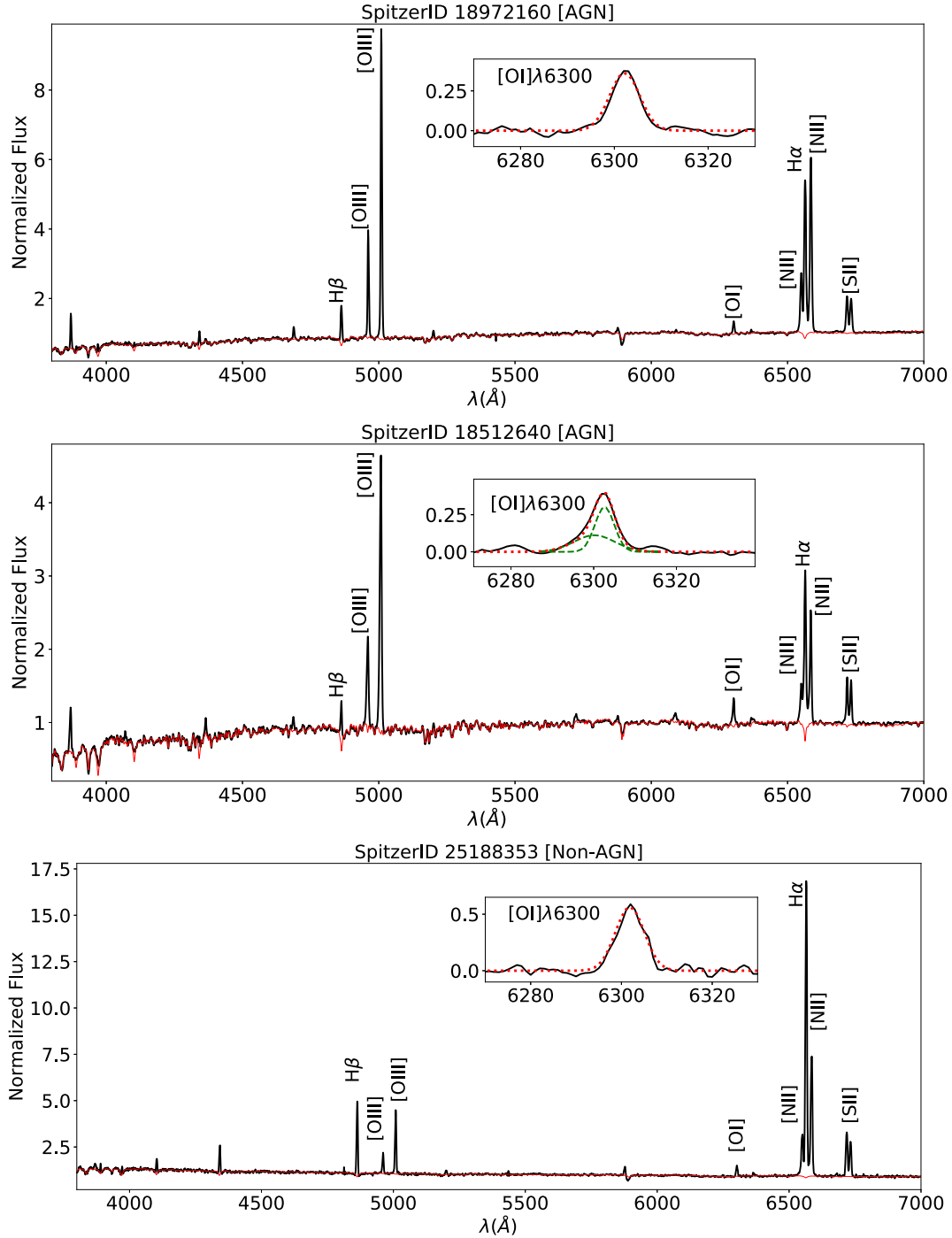
Figure 1. Examples of SDSS spectra for three objects of sample Y. In red, we show the synthesized spectra from STARLIGHT code and the insets show a zoom in the [O I]λ6300 emission-line region from the stellar component subtracted spectra. The resulting fits of the [O I] profiles obtained with IFSCUBE code are shown as dotted red curves and in the middle panel, where the profile is better fitted by two Gaussians, the individual components are shown as dashed green lines. The fluxes are normalized by their values at 5700 Å and the spectra are corrected to the rest frame.

2.2 Stellar population synthesis

The stellar population synthesis is performed using the STARLIGHT code, which is described in Cid Fernandes et al. (2004, 2005). STARLIGHT fits the observed spectrum O_λ with a model spectrum M_λ obtained as a linear combination of $N_\star$ single stellar populations (SSPs). The fitting result is a final population vector **x**, whose components represent the fractional contribution of each SSP to the total synthetic underlying flux at wavelength λ_0 (Cid Fernandes

et al. 2004, 2005). Extinction A_V is modelled as due to a foreground dust layer with the wavelength dependence from Cardelli, Clayton & Mathis (1989). The full model is

$$M_\lambda = M_{\lambda 0} \left[\sum_{j=1}^{N_\star} x_j b_{j,\lambda} r_\lambda \right] \otimes G(v_\star, \sigma_\star), \tag{1}$$

where $M_{\lambda 0}$ is the synthetic flux at the normalization wavelength and $G(v_\star, \sigma_\star)$ is a Gaussian function used to model the line-of-sight stellar velocity distribution centred at velocity $v_\star$ with dispersion $\sigma_\star$. The term x_j is the jth population vector component of the base of elements, defined as $b_{j,\lambda}$. All spectra of the SSP as well as the observed data are normalized to unity at λ_0, so that the reddening term is $r_\lambda = 10^{-0.4(A_\lambda - A_{\lambda 0})}$. The final fit is carried out through a χ^2 minimization procedure.

The base set, e.g. the SSPs used in the fits, is that in the standard STARLIGHT distribution and was taken from Bruzual & Charlot (2003) models. These models provide an adequate spectral and age resolution to fit our data and are widely used in the study of stellar populations in nearby galaxies, which makes the comparison of our results with those of the literature straightforward. In addition, the STARLIGHT code is optimized to run with Bruzual & Charlot (2003) models. The base set and fitting range used are described in Mallmann et al. (2018). It comprises 45 SSPs with 15 ages (0.001, 0.003, 0.005, 0.010, 0.025, 0.040, 0.101, 0.286, 0.640, 0.905, 1.43, 2.50, 5.00, 11.00, and 13.00 Gyr) and three metallicities (0.1, 1, and 2.5 Z$_\odot$). To allow for an AGN component, we also add a featureless component to the base set, represented as a power-law function of the form $F_\lambda \propto \lambda^{-0.5}$ (e.g. Cid Fernandes et al. 2005). The fitting range is between 3800 and 7000 Å with normalization point $\lambda_0 = 5700$ Å. We present examples of the fitting in Fig. 1.

2.3 Emission-line fluxes and kinematics

Fluxes of H$_2$ S(3) 9.665 μm and PAH 11.3 μm features measured from *Spitzer* spectra are available from Lambrides et al. (2018). These fluxes are aperture corrected by flux calibrating *Spitzer* spectra against WISE (Wright et al. 2010) fluxes. Due to the low spectral resolution, no kinematic information of these features is available in *Spitzer* data.

The best-fitting parameters of optical emission lines are from Thomas et al. (2013), who fit the galaxy spectra using the Penalized Pixel-Fitting (PPXF; Cappellari & Emsellem 2004; Cappellari 2017) and Gas and Absorption Line Fitting (GANDALF; Sarzi at al. 2006; Oh et al. 2011) codes to derive the stellar kinematics and emission-line properties. During the fitting, the authors adopt the stellar population models from Maraston & Strömbäck (2011) to represent the continuum/absorption spectra and each emission-line profile is fitted by a single-Gaussian component.

In order to verify whether the distinct fitting and SSP models used by Thomas et al. (2013) and our methods result in similar measurements for the emission lines, we use the IFSCUBE python package[1] to fit the emission-line profiles seen in the residual spectra. The residual spectra are obtained by the subtraction of the continuum/absorption spectra modelled by the STARLIGHT code from the observed spectra. We fit all spectra using single-Gaussian and double-Gaussian functions per line. However, only for ∼5 per cent (14 objects) of our sample, we find that the emission-line fluxes and the velocity dispersion of the broad component exceed 20 per cent of the fluxes and velocity dispersion of the narrow component. The middle panel of Fig. 1 shows an example spectrum, which fulfils these criteria. Since the difference between Thomas et al. (2013) and our measurements is small, we use the emission-line parameters derived from the single-Gaussian fit throughout this paper.

We compare our measurements for [O III]λ5007/Hβ and [N II]λ6583/Hα from the single-Gaussian fit with those of Thomas

et al. (2013) and find that they are very similar, with a mean difference of 0.07 dex for the first ratio and 0.008 dex for the latter. In addition, the IFSCUBE does not provide reliable estimates for the uncertainties. Thus, we use the measurements from Thomas et al. (2013), as they are easily available through the CasJobs server[2] (making our work easy to reproduce) and have been extensively used (e.g. Rembold et al. 2017).

3 RESULTS

We use the physical parameters of the optical and mid-IR emission lines to characterize our sample and to investigate the relation between the molecular gas emission and the ionized gas excitation and kinematics. In Section 3.1, we compare samples Y and N in terms of the optical properties. Section 3.2 presents the relation between the molecular and ionized gas emission, while in Section 3.3 we compare the stellar population and molecular gas properties and Section 3.4 investigates the origin of the molecular gas emission. Unless specified, we use all points of each plot to compute the P_{rank} values throughout this section.

3.1 Comparing the sub-samples

In Fig. 2, we present the [N II]λ6583/Hα versus [O III]λ5007/Hβ emission-line ratio diagnostic (BPT; Baldwin, Phillips & Terlevich 1981) diagrams for all galaxies with data available in the SDSS archive (top panel), for sample Y (middle panel) and for sample N (bottom panel). Objects in the upper right part of the diagram are thought to be dominated by AGN photoionization, and objects in the bottom left dominated by ionization typical of star-forming galaxies.

As we see from the colour density contours in the BPT diagrams, most objects are in the central region, indicating a combination of AGN-dominated and star-forming-dominated ionization. We use the BPT diagram to discriminate our sources as AGNs and non-AGNs throughout this paper. We consider all objects that lie above and right to the line of Kewley et al. (2001) to be AGN dominated. Sample Y (sample N) is composed of 31.3 per cent (32.2 per cent) of AGNs, 22.3 per cent (38.2 per cent) of star-forming galaxies, and 46.4 per cent (29.6 per cent) of transition objects.

The equivalent width of the PAH 6.2 μm feature (EW[PAH]) can be used as an indicator of AGNs (Laurent et al. 2000; Peeters, Spoon & Tielens 2004; Brandl et al. 2006; Sales, Pastoriza & Riffel 2010; Zakamska et al. 2016a). In galaxies where the AGN contribution to the mid-IR emission is larger than 50 per cent, the EW[PAH] is usually smaller than 0.27 μm, while transition objects and star-forming galaxies show EW[PAH] > 0.27 μm (e.g. Lambrides et al. 2018). By comparing the BPT- and EW[PAH]-based AGN classification in our sample, we find that 40 per cent of the optically selected AGNs show EW[PAH] < 0.27 μm and about 65 per cent of the objects classified as AGNs using the EW[PAH] are also classified as AGNs in the optical. Such discrepancies among distinct AGN classification methods are well known (e.g. Heckman & Best 2014).

In Fig. 3, we present the distributions of the [O III]λ5007 luminosity ($L_{\text{[O III]}}$), redshift (z), mean age of the stellar populations weighted by the light, and SFRs derived from the spectral synthesis using the STARLIGHT code over the last 10 Myr. The reported mean

---

[1] https://ifscube.readthedocs.io

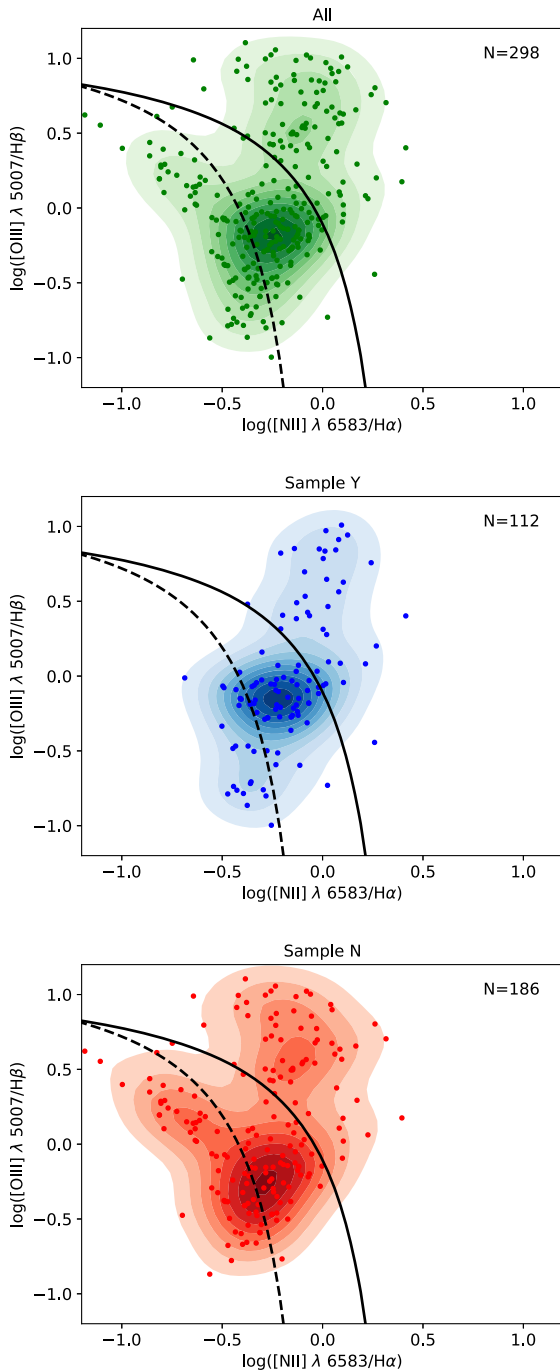[2] http://skyserver.sdss.org/casjobs

Figure 2. BPT diagrams for the galaxies of the *Spitzer* sample with data available in the SDSS. The top panel shows the whole sample, the middle panel is for sample Y, and the bottom panel is for sample N. The continuous line is from Kewley et al. (2001) and the dashed line is from Kauffmann et al. (2003). The number of points (*N*) used in each plot is shown in the top-left corner of the corresponding panel. It is smaller than the size of each sample, as for some objects at least one emission-line flux was not available.

age is calculated following Cid Fernandes et al. (2005):

$$\langle \log t_{\rm L} \rangle = \frac{\sum_{j=1}^{N_\star} x_j \log(t_j)}{\sum_{j=1}^{N_\star} x_j}, \tag{2}$$

where t_j is the age of the template j.

Since our base spectra are in proper units of $\rm L_\odot \, \mathring{A}^{-1} \, M_\odot^{-1}$, and our observed spectra (O_λ) are in units of $\rm erg^{-1} \, s^{-1} \, cm^{-2} \, \mathring{A}^{-1}$, the SFR over the last 10 Myr can be computed assuming that the mass of each base component (j) that has been processed into stars can be defined as

$$M_{\star,j}^{\rm ini} = M_j^{\rm ini} \times \frac{4\pi d^2}{\rm L_\odot}, \tag{3}$$

where $M_{\star,j}^{\rm ini}$ is given in $\rm M_\odot$ and $M_j^{\rm ini}$ is a parameter computed by STARLIGHT and related to the mass that has been converted into stars by jth element and its flux. This parameter is given in $\rm M_\odot \, erg \, s^{-1} \, cm^{-2}$ and d is the distance to the galaxy in cm. Thus, the SFR over the last years can be obtained by the following equation:

$$\rm SFR = \frac{\sum_{j_i}^{j_f} M_{\star,j}^{\rm ini}}{t_{j_f} - t_{j_i}}. \tag{4}$$

To obtain SFR over the last 10 Myr, we consider only the elements with ages $t \leq 10 \, \rm Myr$ (e.g. $j_f = 10 \, \rm Myr$ and $j_i = 0$).

We observe that sample Y and sample N show similar distributions of $L_{\rm [O\,III]}$, suggesting that the presence or absence of rotational $\rm H_2$ emission lines is not related to the power of the radiation field. The estimated $P_{\rm KS}$ confirms that the $L_{\rm [O\,III]}$ distributions of both samples are statistically equivalent. The redshift distributions of the sub-samples are statistically distinct, as indicated by the small $P_{\rm KS}$. On average, galaxies from sample N are located farther away than objects of sample Y, which could explain the non-detection of weak molecular lines in sample N in the farther objects.

The bottom panels of Fig. 3 show that the mean ages of the stellar populations of sample Y and sample N are similar, whereas the distributions of SFRs are distinct ($P_{\rm KS} = 0.022$). Sample Y displays larger values of SFR. As the SFR correlates with the amount of gas available to form stars, a possible interpretation of this result is that galaxies from sample Y present a larger gas reservoir than objects of sample N, suggesting that the detection of the molecular lines is closely related to the presence of molecular gas.

However, sample N is composed of objects, on average, farther away as compared to sample Y. Therefore, the apparent difference in SFR could also be due to the fact that it is more difficult to properly measure the SFR for the more distant sample N. In order to address this problem, we follow Zakamska et al. (2004) and redshift-weight SFR distributions of samples Y and N for a more direct comparison. To this end, we divide both samples in 11 bins of z (the same number of bins used to construct the SFR histograms) and assign a weight w to each object of sample N:

$$w = \frac{n_i N_{\rm Y}}{m_i N_{\rm N}}, \tag{5}$$

where n_i and m_i are the number of objects from samples Y and N in each redshift bin, respectively. $N_{\rm Y}$ and $N_{\rm N}$ are the total number of objects from each bin. The resulting weighted SFR distribution of sample N is shown as a dashed green line in bthe ottom-right panel of Fig. 3 and indeed it is more similar to that of sample Y. We compute $P_{\rm KS} = 0.095$, indicating that there is no statistically significant difference between the SFR distributions in sample Y and weighted sample N.

In summary, the main differences between samples Y and N are as follows: sample Y composed of objects at smaller z shows a higher fraction of transition objects and a smaller fraction of star-forming galaxies in comparison to sample N. Thus, possible explanations for the non-detection of molecular lines in sample N are that these lines may be too weak to be detected in the farther objects or they are related to the AGN physics, rather than to star formation.
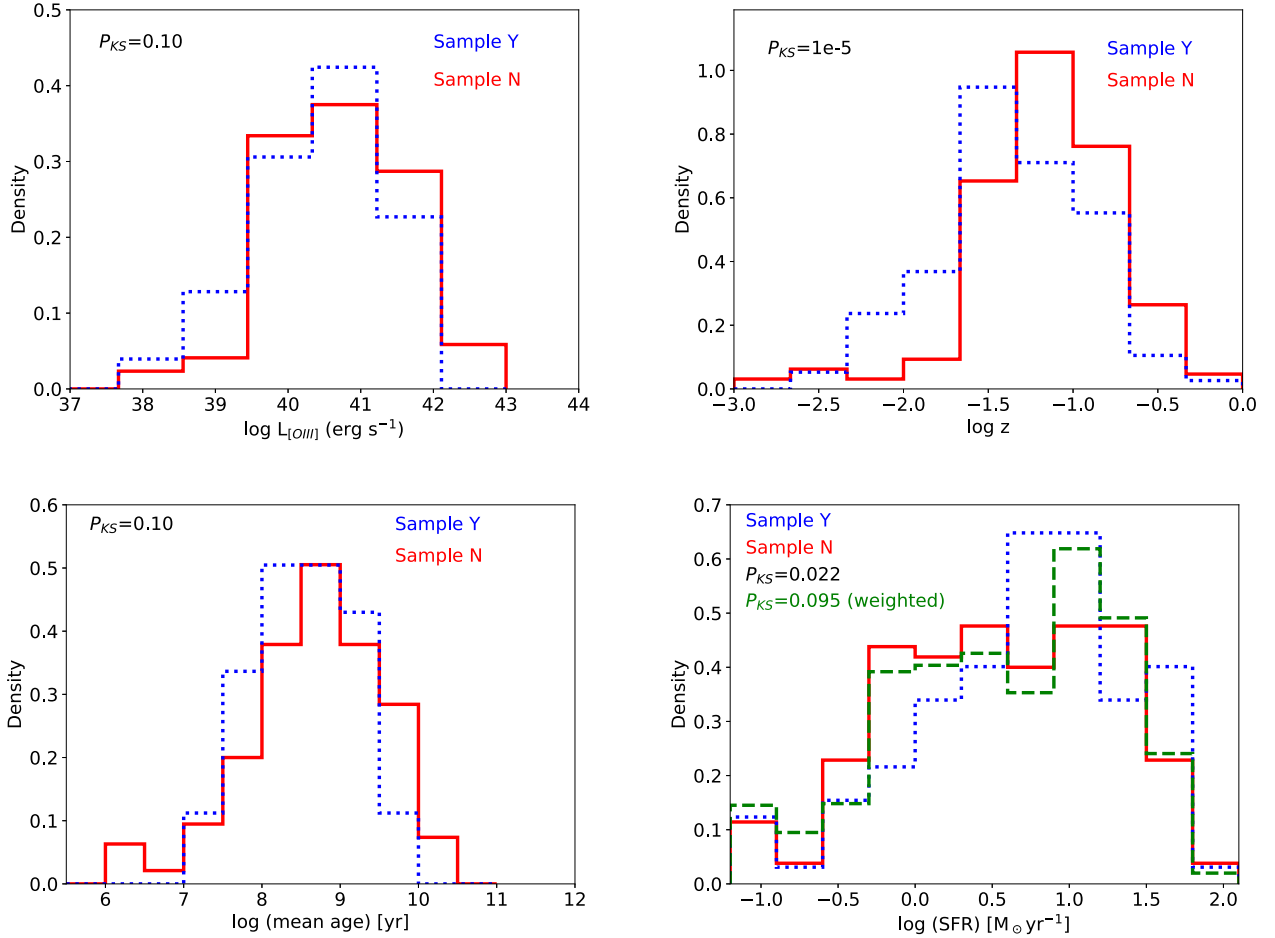
Figure 3. Comparison of samples Y and N in terms of the [O III]λ5007 luminosity (top left), redshift (top right), mean age of the stellar populations (bottom left), and SFR during the last 10 Myr (bottom right). The P_{KS} values are shown in each panel. The green dashed line shows the distribution of SFR of sample N, weighted by the redshift distribution (see text).

3.2 The relation between molecular and ionized gas emission

In this section, we explore the properties of the ionized gas in relation to the H$_2$ S(3) 9.665 μm/PAH 11.3 μm emission-line ratio. For star-forming galaxies, the H$_2$/PAH ratio is approximately constant as both lines are produced in photodissociation regions (Roussel at al. 2007). We indeed find that H$_2$ S(3) and PAH luminosities correlate for sample Y, and AGNs show smaller values in both parameters. The larger typical PAH values in star-forming galaxies are likely due to a selection effect that starburst galaxies (with high SFRs) were more likely to be selected for follow-up *Spitzer* spectroscopy. Indeed, the median PAH λ11.3 μm luminosity in sample N [log(PAH) = 42.5] is slightly higher than that in sample Y [log(PAH) = 42.2].

We also find that the H$_2$/PAH ratio is larger in AGNs and we refer to these higher values as 'H$_2$ excess'. In AGN hosts, an excess in the H$_2$ emission is observed relative to the PAH emission (Rigopoulou et al. 2002; Zakamska 2010; Ogle et al. 2012; Hill & Zakamska 2014; Stierwalt et al. 2014; Lambrides et al. 2018; Petric et al. 2018). We find average values for the H$_2$ S(3) 9.665 μm/PAH 11.3 μm ratio of $(1.76 \pm 0.23) \times 10^{-2}$ for star-forming galaxies, $(9.51 \pm 2.97) \times 10^{-2}$ for AGN hosts, and $(6.99 \pm 2.67) \times 10^{-2}$ for transition objects. Thus, in AGN hosts we find that the H$_2$/PAH is about five times larger than that in star-forming galaxies.

Fig. 4 shows the relationships between [O III]λ5007/Hβ (left-hand panel), [O I]λ6300/Hα (right-hand panel), and H$_2$ S(3)/PAH. [O III]λ5007/Hβ is a tracer of the radiation field, while [O I]λ6300/Hα is a tracer of shocks in neutral gas (e.g. Allen et al. 2008; Ho et al. 2014). As indicated by the P_{rank} values, we find that both optical line ratios correlate with the H$_2$ S(3)/PAH ratio, but a better correlation is found for [O I]/Hα, which may indicate that neutral gas shocks play an important role in the production of the observed H$_2$ excess.

In order to determine whether there is a kinematic signature of the shocks that may yield the H$_2$ excess, we plot the velocity dispersion (σ) of [O III]λ5007 and [O I]λ6300 against H$_2$ S(3) 9.665 μm/PAH 11.3 μm. The corresponding plots are shown in Fig. 5. Both [O III]λ5007 and [O I]λ6300 velocity dispersions are correlated with the H$_2$ S(3)/PAH ratio, but as for the emission-line ratios, a better correlation is found for the [O I] emission line.

3.3 Molecular gas emission and stellar populations

In the left-hand panel of Fig. 6, we show the mean age of the stellar populations, weighted by their contributions to the observed continuum emission, versus the H$_2$ S(3)/PAH emission-line ratio.

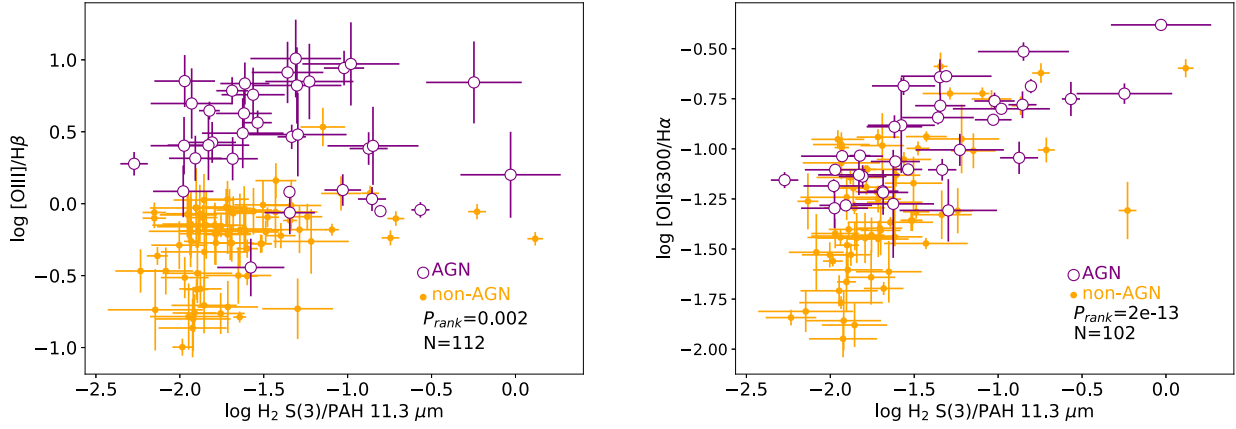**Figure 4.** [O III]λ5007/H β (left-hand panel) and [O I]λ6300/H α (right-hand panel) versus H₂ S(3) 9.665 μm/PAH 11.3 μm emission-line ratios. AGNs are shown as open circles and non-AGNs as filled circles. The $P_{\rm rank}$ values are indicated in each plot.
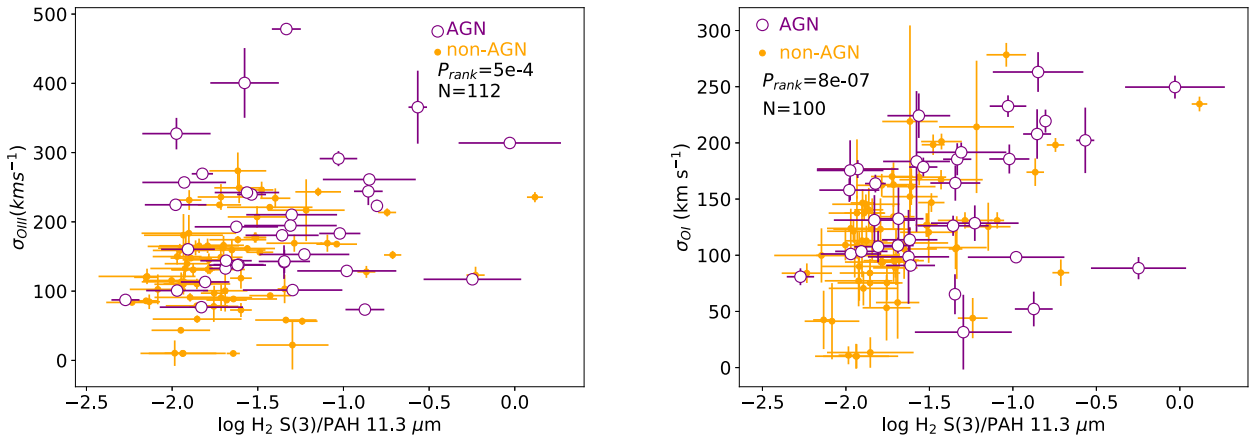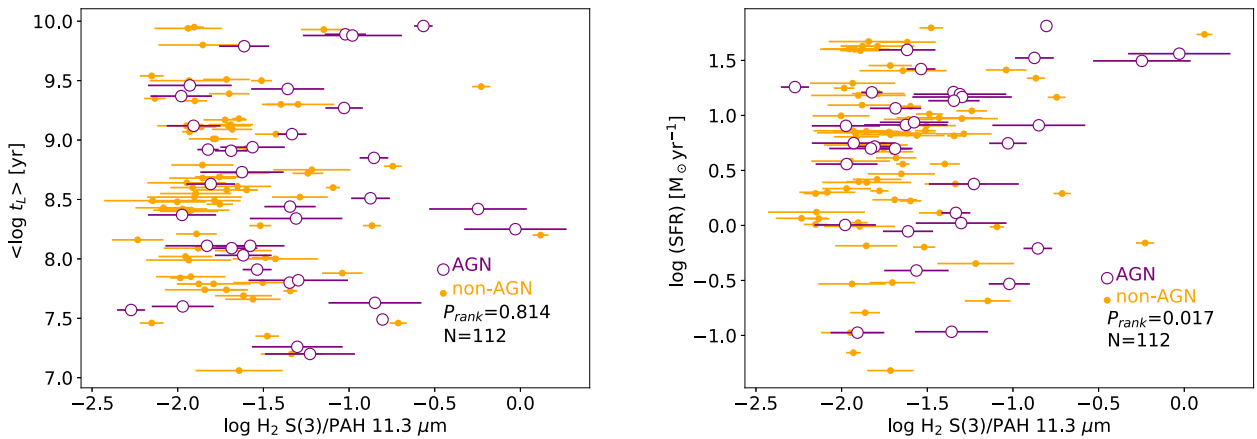

Figure 5. Plots of [O III]λ5007 (left-hand panel) and [O I]λ6300 (right-hand panel) velocity dispersion versus H₂ S(3) 9.665 μm/PAH 11.3 μm emission-line ratios. AGNs are shown as open circles and non-AGNs as filled circles. The $P_{\rm rank}$ values are indicated in each plot.

Figure 6. Mean age of the stellar populations (left) and SFR (right) versus H₂ S(3) 9.665 μm/PAH 11.3 μm emission-line ratios. AGNs are shown as open circles and non-AGNs as filled circles. The $P_{\rm rank}$ value and the number of points are indicated in each plot.

As indicated by the derived $P_{\rm rank}$ values, these parameters are not correlated. In the right-hand panel, we use the SFR over the last 10 Myr instead of the mean age. The resulting $P_{\rm rank}$ value suggests that the parameters are correlated.

Previous studies found that the H₂/PAH ratio is approximately constant for star-forming galaxies (Roussel at al. 2007), which is in apparent discrepancy with the correlation between SFR and H₂/PAH. We find mean values of $\langle \log H_2/PAH \rangle = -1.37 \pm 0.08$

and $\langle \log H_2/PAH \rangle = -1.65 \pm 0.05$ for AGNs and non-AGNs, respectively. By computing the P_{rank} values between SFR and H_2/PAH, we do not find a statistically significant correlation for the non-AGN sample ($P_{\mathrm{rank}} = 0.16$), while SFR and H_2/PAH correlate for the AGN sample ($P_{\mathrm{rank}} = 0.04$). This indicates that the correlation seen for the whole sample is mainly due to the AGN, rather than the non-AGN sources. A possible interpretation for the correlation between SFR and H_2/PAH in the AGN sample is that the same gas that triggers the star formation also triggers the AGN activity, connecting both processes (Perry & Dyson ; Terlevich & Melnick 1985; Norman & Scoville 1988; Cid Fernandes et al. 2001; Riffel et al. 2009; Mallmann et al. 2018).

The absence of a correlation for non-AGNs indicates that the origin of the H_2 emission excess is related to the AGNs, rather than to star formation, in agreement with Lambrides et al. (2018). In addition, our results suggest that shocks due to AGN winds are present as indicated by the high [O I] velocity dispersion in some of the objects in our sample. As expected, shocks contribute H_2 excitation over what is expected from star formation alone, which leads to the correlation between H_2/PAH and [O I] velocity dispersion in Fig. 5. Furthermore, the fact that there exists a correlation between S(3)/S(1) and the [O I] velocity dispersion (Fig. 7) indicates that the H_2 excitation temperatures are coupled to the excitation mechanism and may be potentially used as shock diagnostics. This leads to the conclusion that the way AGNs impact the interstellar medium is mainly due to mechanical feedback, instead of radiative feedback.

3.4 Gas kinematics and molecular gas emission

In order to further investigate the impact of the AGNs in the interstellar medium, in Fig. 5 we examine the H_2 S(3) 9.665 μm/H_2 S(1) 17.03 μm emission-line ratio against the [O I]λ6300 velocity dispersion. The former is a tracer of the H_2 excitation temperature. As this ratio increases, the temperature also increases. The latter can be tracing the gravitational potential of the galaxy but can also be an indicator of shocks. A way to determine whether the [O I]λ6300 velocity dispersion is tracing the gravitational potential is by comparing it with the stellar velocity dispersion ($\sigma_\star$). The stellar velocity dispersions of the galaxies in our sample are available from Thomas et al. (2013). Following Ilha et al. (2019), we quantify the differences between the stellar and [O I] velocity dispersions using the parameter f_σ:

$$f_\sigma = \frac{\sigma_{[\mathrm{O\,I}]} - \sigma_\star}{\sigma_\star}. \tag{6}$$

Higher values of f_σ are indicative of a disturbed kinematics (e.g. the gas motions are inconsistent with the gravitational potential of the galaxy) and most probably due to outflows. This is further supported by the fact that for 70 per cent (10/14) of the objects that show emission lines with more than one kinematic component, the broad component is blueshifted by a few tens of km s^{-1}. Excess blueshift is a classical signature of outflows (Whittle 1985) since the receding redshifted part of the outflow tends to have a greater extinction than the blueshifted part. Similar disturbed gas kinematics can also be produced by gas inflows towards the centre of the galaxies, but this scenario is unlikely in our sample, as inflows are usually associated with low-velocity dispersion gas (Storchi-Bergmann & Schnorr-Müller 2019).

Ilha et al. (2019) report median values of f_σ for AGNs and inactive galaxies of 0.04 and −0.23, respectively, based on measurements for [O III]λ5007 instead of [O I]λ6300. They conclude that the higher
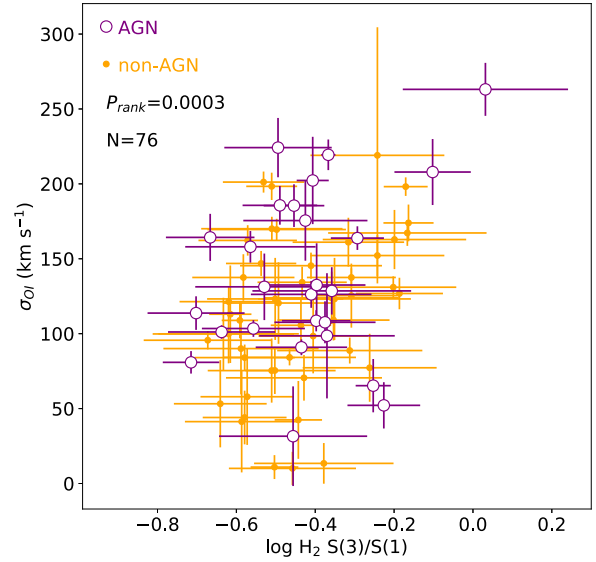

Figure 7. H_2 S(3) 9.665 μm/H_2 S(1) 17.03 μm emission-line ratio versus the [O I]λ6300 velocity dispersion. AGNs (non-AGNs) are shown as open (filled) circles, and the number of objects and the P_{rank} value are indicated in the panel.

values seen for AGNs are due to gas outflows. For our sample, we find that AGNs and non-AGNs have similar $\sigma_\star$ distributions (P_{KS} = 0.93) and $\langle f_\sigma \rangle = 0.24 \pm 0.07$ for AGNs, 0.13 ± 0.06 for transition objects, and −0.24 ± 0.07 for star-forming galaxies. These values indicate a contribution of shocks to the [O I]λ6300 emission from AGNs and transition objects, possibly due to AGN-driven winds.

Fig. 7 shows the H_2 S(3) 9.665 μm/H_2 S(1) 17.03 μm ratio against the [O I]λ6300 velocity dispersion. Although the uncertainties in H_2 S(3) 9.665 μm/H_2 S(1) 17.03 μm ratio for individual sources are large, we find a correlation, with $P_{\mathrm{rank}} = 3 \times 10^{-4}$. In addition, AGNs present on average higher [O I] σ values. This indicates that AGNs play an important role in the production of the H_2 emission, supporting the results of Lambrides et al. (2018). A similar behaviour is observed if we plot f_σ on the y-axis, but the uncertainties in f_σ are high.

We compare the [O III] and [O I] velocity dispersions for the galaxies of our sample. As mentioned in Section 3.1, the detection of the molecular lines seems to be more related to the presence of a gas reservoir in the centre of the galaxies, rather than to the radiation field. Thus, in the comparison of [O III] and [O I] velocity dispersions, we include the whole sample, instead of only those galaxies with detected molecular lines. A correlation is found between [O III] and [O I] σ values, but [O III] presents systematically higher velocity dispersion than [O I]. The f_σ values for [O III] are also higher than those for [O I]. A possible interpretation for this result is that [O III] and [O I] trace distinct phases of the outflow.

We find that both $L_{[\mathrm{O\,III}]}$ and SFR correlate with the [O I]λ6300 velocity dispersion, in agreement with previous works (Woo, Son & Bae 2017; Ilha et al. 2019; Yu et al. 2019). In star-forming galaxies, gravitational instabilities alone cannot explain the observed gas velocity dispersion and stellar winds are required to produce the correlation between SFR and σ (Yu et al. 2019). Similar results are found for AGNs, while non-AGNs show lower values for both parameters (Woo et al. 2017; Ilha et al. 2019).

4 DISCUSSION

4.1 Relationship between outflow phases

Galactic outflows are a multiphase phenomenon (Riffel et al. 2006, 2019; Feruglio et al. 2010; Veilleux et al. 2013; Zakamska et al. 2016b; González-Alfonso et al. 2017; Shimizu et al. 2019), with different diagnostics suitable for the different phases. The relationship between the phases of the outflow is not well understood, and it is not yet known which phase carries most of the mass, momentum, and energy of the outflow. Our paper addresses these important questions by examining the relationships between mid-IR diagnostics of star formation (PAHs) and warm molecular gas (rotational H_2 lines) on the one hand and optical emission lines associated with neutral and ionized gas phases on the other hand.

We find that both [O III]λ5007/Hβ and [O I]λ6300/Hα correlate with the H_2 S(3) 9.665 μm/PAH 11.3 μm line ratio (Fig. 4), but a much better correlation is found for the latter. Similarly, we find a stronger correlation between H_2/PAH and the kinematics of [O I] than we do with the kinematics of [O III]. Our findings suggest in galaxies with H_2 excess, [O I] and [O III] emission lines are emitted by gas that is not in dynamical equilibrium with the host galaxy. Additionally, because the correlations between H_2 and [O I] are tighter than those between H_2 and [O III], we infer that the neutral and warm molecular gas phases are much more strongly coupled to each other than they are to the [O III]-emitting ionized gas.

The same observations indicate that shocks are playing an important role in producing the H_2 emission. Indeed, H_2 is strongly correlated with [O I], and [O I]/Hα is a known tracer of shocks (Monreal-Ibero, Arribas & Colina 2006; Monreal-Ibero et al. 2010; Rich, Kewley & Dopita 2011, 2014, 2015; Ho et al. 2014). If the velocity dispersion of [O I] is larger than 150 km s^{-1} and log [O I]λ6300/H$\alpha \gtrsim -1.0$, shocks with velocities in the range of 160–300 km s^{-1} are the dominant excitation mechanism of [O I]. For smaller σ and line ratio values, both shocks and photoionization contribute to the gas excitation (Ho et al. 2014).

Furthermore, not only are the shocks responsible for the H_2 excess, but given the strength of the correlation between all measures of H_2 and [O I], it suggests that the excess H_2 is produced in the same clouds as those that produce [O I]. This is somewhat surprising because we normally think of neutral medium and dense molecular clouds as being two different components of the interstellar medium, and in particular star-forming molecular clouds in the Milky Way are much denser than the diffuse neutral component. Multiple numerical simulations demonstrated that dense molecular clouds would be very difficult to accelerate by an incoming wind (Klein, McKee & Colella 1994; Scannapieco & Brüggen 2015; Brüggen & Scannapieco 2016; Zhang et al. 2017). Instead, such clouds would shred and become entrained in the wind. Therefore, to explain the presence of recently discovered AGN-driven molecular outflows, theoretical models (Richings & Faucher-Gière 2018a, b) suggest that molecules can form within the already accelerated outflow. Possibly this is what we are seeing in both [O I] and H_2.

The better correlations found for [O I] with the H_2/PAH indicate that the H_2 and [O I] emissions arise from similar outflow phases, while [O III] originates from a higher velocity outflowing gas. This interpretation is consistent with results found for ULIRGs, which show a good correlation between [O I]λ6300/Hα and H_2/PAH ratios, but the higher values of H_2/PAH seen in AGNs cannot only be explained by the gas excitation due to the AGN radiation field, and shocks are necessary to explain the correlation (Roussel at al. 2007; Hill & Zakamska 2014).

Our sample is composed mostly of low-luminosity AGNs (L_{bol} = 10^{42}–10^{45} erg s^{-1}) and the kinematics suggest that most of the gas is in equilibrium with the galaxy and only a small fraction may be outflowing. As the wind velocities from low-luminosity AGNs are expected to be small, to disentangle the gravitational and wind components using single-aperture spectra is not an easy task and still remains unresolved. We assume that there are no outflows in the non-AGN sample, and that the increased line widths in AGNs are due to the outflowing gas. Thus, we use the difference between the median line widths for AGNs and non-AGNs as a proxy of the velocity of the outflow (v_{out}). We measure $v_{out}^{[O\ III]} \sim 100$ km s^{-1} for the [O III] and $v_{out}^{[O\ I]} \sim 77$ km s^{-1} for the [O I] outflow components, respectively. This is a very simplistic approach, which does not take into account possible differences in the mass distribution of AGN and non-AGN hosts in our sample. However, Ilha et al. (2019) find that AGNs show higher values of gas velocity dispersion compared to inactive galaxies, matched by the AGN host properties, which include the morphological classification and stellar mass. They quantify this difference by the f_σ parameter and interpret the higher values being due to unresolved AGN outflows. In addition, the derived mean outflow velocity in our sample is consistent with the values obtained from spatially resolved observations (Cresci et al. 2015; Kakkad et al. 2016; Diniz et al. 2019; Slater et al. 2019)

We find that [O III] shows systematically higher velocity dispersion than [O I]. This suggests that [O I] and [O III] trace not only distinct gas phases, but also distinct phases of the outflow, and the relationship between [O III]] and [O I] velocities is qualitatively consistent with [O III] tracing lower density gas than [O I], as expected – the critical densities to produce the [O III]5007 and [O I]6300 lines are 7×10^5 and 2×10^6 cm^{-3}, respectively (Osterbrock & Ferland 2006).

If the outflows result in shocks propagating from one phase to another, the densities and velocities of the different phases are related by $n_{[O\ III]}(v_{out,\ [O\ III]})^2 = n_{[O\ I]}(v_{out,\ [O\ I]})^2$. This implies that density of the [O I] clouds is a factor 1.7 higher than that of the [O III] clouds. This result is consistent with theoretical predictions based on multicomponent photoionization models of the narrow-line region (Komossa & Schulz 1997). Assuming that the density of the clouds that produce the [O III] emission is 500 cm^{-3} – a typical value of the electron density measured for AGNs based on the [S II] emission lines (Dors et al. 2014) – we obtain $n_{[O\ I]} \approx 850$ cm^{-3}. This value is smaller than the critical density for collisional de-excitation of the H_2 S(3) level of $\sim 10^4$ cm^{-3} (Roussel at al. 2007), and thus is consistent with our interpretation that the H_2 emission excess is likely produced by the same clouds that produce [O I]λ6300. However, the nature of the outflows may be much more complex than our simple approach, as we are not able to properly constrain the geometries and gas densities of the outflows from single-aperture spectra. Although the adopted value of n_e is consistent with those derived for spatially resolved outflows using the [S II] emission lines (Lena et al. 2015, 2016; Couto et al. 2016; Soto-Pinto et al. 2019), recent results suggest that the [S II]-based densities of ionized outflows can be underestimated by up to two orders of magnitude (Baron & Netzer 2019b).

4.2 Energetics of the molecular outflows

Our results indicate that shocks appear to play an important role in the production of both H_2 and [O I]λ6300 emissions. Theoretical models show that H_2 emission can be produced by shocks with velocities from 30 to 150 km s^{-1} (Hollenbach & McKee 1989), while the shocks with velocities in the range 100–300 km s^{-1} produce

[O I] emission (Ho et al. 2014). These values are smaller than the wind velocities (480–1500 km s^{-1}) derived from hydrodynamical simulations of wind production from low-luminosity AGNs in subparsec scales (Almeida & Nemmenn 2019). Considering that the particles launched from the accretion disc are expected to decelerate due to the gravitational interaction at larger distances from the AGNs, they can be responsible to produce the shocks needed to produce the H$_2$ and [O I] emission.

Assuming a biconical geometry for the molecular outflow, we can estimate the mass outflow rate through a circular cross-section with radius r as $\dot{M}_{H_2} = 4\pi m_p f n_{H_2} v_{H_2} r^2$, where m_p is the proton mass, f is the filling factor, n_{H_2} is the H$_2$ number density, and v_{H_2} is the velocity of the H$_2$ outflow. Assuming a typical value for bicone opening angle of 45$°$ (Müller Sánchez et al. 2011) to calculate r, $n_{H_2} = 850$ cm^{-3} (as estimated for the [O I] clouds), $f = 0.01$ (a typical value estimated for Sy galaxies; Storchi-Bergmann et al. 2010; Schnorr-Müller et al. 2014), and $v_{H_2} \approx 77$ km s^{-1} (as estimated for [O I]), the outflow rate at 200 pc from the nucleus is $\dot{M}_{H_2} \approx 1.6$ M$_\odot$ yr^{-1}. We calculate the outflow rate at this distance because it corresponds to the peak of the location of the outflows in a sample of $\sim$4000 type 2 AGNs (Baron & Netzer 2019a). The derived mass outflow rate is consistent with those obtained from spatially resolved observations of outflows in nearby AGNs (e.g. Diniz et al. 2019; Shimizu et al. 2019).

The kinetic power of the outflow is $\dot{E}_{out} = (1/2)\dot{M}_{H_2} v_{H_2}^2 \approx 2.8 \times 10^{39}$ erg s^{-1}. The median [O III]λ5007 luminosity of the AGNs in our sample is $\langle L_{[O III]} \rangle = 5.7 \times 10^{40}$ erg s^{-1}. Using a bolometric correction to the [O III]5007 luminosity of a factor of 3500 (Heckman & Best 2004), the corresponding bolometric luminosity is $L_{bol} \approx 2 \times 10^{44}$ erg s^{-1}. Thus, the kinetic power of the outflow is negligible compared to the AGN bolometric luminosity, meaning that there is no important feedback effect on the host galaxies.

The estimated velocities of warm molecular, neutral, and ionized gases are $\lesssim$100 km s^{-1}, being smaller than the escape velocities of the galaxies of our sample. This implies a 'maintenance mode' feedback, in which the gas is outflowing from the nucleus, but is redistributed within the galaxies remaining available for further star formation. This result is similar to that found in other low-luminosity AGNs (e.g. Diniz et al. 2019) and ULIRGs (e.g. Emonts et al. 2017). Indeed, the power of the AGN outflows is strongly correlated with AGN luminosity (Fiore et al. 2017). In powerful AGNs, such as luminous quasars, the velocity ($\gtrsim$1000 km s^{-1}) and kinetic power ($\times$ few L_{bol}) of the outflow are much higher and then the 'blow-out' mode feedback takes place (Di Matteo, Springel, Hernquist 2005; Hopkins & Elvis 2010; Storchi-Bergmann et al. 2010; Hopkins et al. 2012; Zakamska et al. 2016b; Shimizu et al. 2019), in which the gas is expelled out of the galaxy.

5 CONCLUSIONS AND IMPLICATIONS

In this work, we match the sample of galaxies with mid-IR spectra available in the *Spitzer Space Telescope* archive, compiled by Lambrides et al. (2018), with optical spectroscopic observations from the SDSS archive. From the 2015 galaxies with mid-IR spectra, we find that 309 have SDSS spectra. This sample is used to investigate the origin of the excess of molecular hydrogen emission observed the mid-IR in nearby AGN host galaxies. By comparing mid-IR emission-line ratios with stellar population properties, optical emission-line ratios, and gas kinematics, we conclude that shocks play a major role in the production of the H$_2$ emission. These shocks are mainly due to AGN-driven winds.

We find strong correlations between H$_2$ fluxes and excitation temperatures and [O I] fluxes and kinematics. Although similar relationships are also apparent between H$_2$ and [O III], these correlations are weaker. We interpret these relationships as evidence of AGN molecular outflows that we are indirectly uncovering using the [O I] emission, which is a reliable tracer of shocks in neutral material.

We find that objects with the strongest [O I]λ6300/Hα and highest velocity dispersions in [O I] are the most likely hosts of molecular outflows. In order to confirm our hypothesis, these objects should be observed directly to get spatially resolved kinematics of the near-IR rovibrational H$_2$ lines (which can be done using 10 m class ground-based telescopes), mid-IR rotational lines (can be done with JWST), and other molecular lines with ALMA to trace all different components of the outflow (hot, warm, and cold).

REFERENCES

Aguado D. S. et al., 2019, ApJS, 240, 23
Alexander D. M., Hickox R. C., 2012, New Astron. Rev., 56, 93
Allen M. G., Groves B. A., Dopita M. A., Sutherland R. S., Kewley L. J., 2008, ApJS, 178, 20
Almeida I., Nemmenn R. S., 2019, MNRAS, preprint (arXiv:1905.13708)
Alonso-Herrero A. et al., 2019, A&A, 628, A65
Arribas S., Colina L., Bellocchi E., Maiolino R., Villar-Martín M., 2014, A&A, 568, A14
Baldwin J. A., Phillips M. M., Terlevich R., 1981, PASP, 93, 5
Baron D., Netzer H., 2019a, MNRAS, 482, 3915
Baron D., Netzer H., 2019b, MNRAS, 486, 4290
Blanton M. R. et al., 2017, AJ, 154, 28
Brandl B. R. et al., 2006, ApJ, 653, 1129
Brüggen M., Scannapieco E., 2016, ApJ, 822, 31
Bruzual G., Charlot S., 2003, MNRAS, 344, 1000
Cappellari M., 2017, MNRAS, 466, 798
Cappellari M., Emsellem E., 2004, PASP, 116, 138

Cardelli J. A., Clayton G. C., Mathis J. S., 1989, ApJ, 345, 245
Carniani S. et al., 2015, A&A, 580, A102
Cattaneo A. et al., 2009, Nature, 460, 213
Cid Fernandes R., Heckman T., Schmitt H., Gonzlez Delgado R. M., Storchi-Bergmann T., 2001, ApJ, 558, 81
Cid Fernandes R., Gu Q., Melnick J., Terlevich E., Terlevich R., Kunth D., Rodrigues Lacerda R., Joguet B., 2004, MNRAS, 355, 273
Cid Fernandes R., Mateus A., Sodré L., Stasińska G., Gomes J. M., 2005, MNRAS, 358, 363
Combes F. et al., 2013, A&A, 558, A124
Conselice C. J., 2014, ARA&A, 52, 291
Couto G. S., Storchi-Bergmann T., Robinson A., Riffel R. A., Kharb P., Lena D., Schnorr-Müller A., 2016, MNRAS, 458, 855
Cresci G. et al., 2015, A&A, 582, A63
Davies R. I. et al., 2014, ApJ, 792, 101
Di Matteo T., Springel V., Hernquist L., 2005, Nature, 433, 604
Diniz M. R., Riffel R. A., Stochi-Bergmann T., Riffel R., 2019, MNRAS, 487, 3958
Dors O. L., Cardaci M. V., Hägele G. F., Krabbe Â. C., 2014, MNRAS, 443, 1291
Durré M., Mould J., 2019, ApJ, 870, 37
Emonts B. H. C., Colina L., Piqueras-López J., Garcia-Burillo S., Pereira-Santaella M., Arribas S., Labiano A., Alonso-Herrero A., 2017, A&A, 607, A116
Fabian A. C., 2012, ARA&A, 56, 93
Feruglio C., Maiolino R., Piconcelli E., Menci N., Aussel H., Lamastra A., Fiore F., 2010, A&A, 518, L155
Fiore F. et al., 2017, A&A, 601, A143
Fischer J. et al., 2010, A&A, 518, L41
Fischer T. C. et al., 2017, ApJ, 834, 30
Gallagher R., Maiolino R., Belfiore F., Drory N., Riffel R., Riffel R. A., 2019, MNRAS, 485, 3409
García-Burillo S. et al., 2014, A&A, 567, A125
González-Alfonso E. et al., 2014, A&A, 561, A27
González-Alfonso E. et al., 2017, ApJ, 836, 11
Gunn J. E. et al., 2006, AJ, 131, 2332
Harrison C. M., 2017, Nat. Astron., 1, 0165
Hatfield P. W., Jarvis M. J., 2017, MNRAS, 472, 3570
Heckman T. M., Best P. N., 2014, ARA&A, 52, 589
Heckman T. M., Kauffmann G., Brinchmann J., Charlot S., Tremonti C., White S. D. M., 2004, ApJ, 613, 109
Hill M. J., Zakamska N. L., 2014, MNRAS, 439, 2701
Ho T. et al., 2014, MNRAS, 444, 3894
Hollenbach D., McKee C. F., 1989, ApJ, 342, 306
Hopkins P. F., Elvis M., 2010, MNRAS, 401, 7
Hopkins P. F., Hayward C. C., Narayanan D., Hernquist L., 2012, MNRAS, 420, 320
Husemann B. et al., 2019, A&A, 627, A53
Ilha G. S. et al., 2019, MNRAS, 484, 252
Imanishi M., Nakanishi K., Izumi T., 2018, ApJ, 856, 143
Imanishi M., Nakanishi K., Izumi T., 2019, ApJS, 241, 19
Kakkad D. et al., 2016, A&A, 592, A148
Kauffmann G. et al., 2003, MNRAS, 346, 1055
Kewley L. J., Dopita M. A., Sutherland R. S., Heisler C. A., Trevena J., 2001, ApJ, 556, 121
Kim K., Malhotra S., Rhoads J. E., Joshi B., Fererras I., Pasquali A., 2018, ApJ, 867, 118
Klein R. I., McKee C. F., Colella P., 1994, ApJ, 420, 213
Komossa S., Schulz H., 1997, A&A, 323, 31
Lambrides E. L., Petric A. O., Tchernyshyov K., Zakamska N. L., Watts D. J., 2019, MNRAS, 487, 1823
Laurent O., Mirabel I. F., Charmandaris V., Gallais P., Madden S. C., Sauvage M., Vigroux L., Cesarsky C., 2000, A&A, 359, 887
Lena D. et al., 2015, ApJ, 806, 84
Lena D., Robinson A., Storchi-Bergmann T., Couto G. S., Schnorr-Müller A., Riffel R. A., 2016, MNRAS, 459, 4485
Liu G., Zakamska N. L., Greene J. E., Nesvadba N. P. H., Liu X., 2013, MNRAS, 430, 2327
Liu Q., Wang E., Lin Z., Gao Y., Liu H., Berhane Teklu B., Kong X., 2018, ApJ, 857, 17
Mallmann N. D. et al., 2018, MNRAS, 478, 5491
Maraston C., Strömbäck G., 2011, MNRAS, 418, 2785
May D., Rodríguez-Ardila A., Prieto M. A., Fernández-Ontiveros J. A., Diaz Y., Mazzalay X., 2018, MNRAS, 481, L105
Mazzalay X. et al., 2014, MNRAS, 438, 2036
Monreal-Ibero A., Arribas S., Colina L., 2006, ApJ, 637, 138
Monreal-Ibero A., Arribas S., Colina L., Rodríguez-Zaurín J., Alonso-Herrero A., García-Marín M., 2010, A&A, 517, A28
Morganti R., Oosterloo T., Oonk J. B. R., Frieswijk W., Tadhunter C., 2015, A&A, 580, A1
Müller Sánchez F., Davies R. I., Genzel R., Tacconi L. J., Eisenhauer F., Hicks E. K. S., Friedrich S., Sternberg A., 2009, ApJ, 691, 749
Müller Sánchez F., Prieto M. A., Hicks E. K. S., Vives-Arias H., Davies R. I., Malkan M., Tacconi L. J., Genzel R., 2011, ApJ, 739, 69
Norman C., Scoville N., 1988, ApJ, 332, 124
Ogle P., Davies J. E., Appleton P. N., Bertincourt B., Seymour N., Helou G., 2012, ApJ, 751, 13
Oh K., Sarzi M., Schawinski K., Yi S. K., 2011, ApJS, 195, 13
Osterbrock D. E., Ferland G. J., 2006, Astrophysics of Gaseous Nebulae and Active Galactic Nuclei, 2nd edn. Univ. Science Books, Mill Valley, CA
Peeters E., Spoon H. W. W., Tielens A. G. G. M., 2004, ApJ, 613, 986
Pereira-Santaella M. et al., 2018, A&A, 616, A171
Petric A. O. et al., 2018, AJ, 156, 295
Ramakrishnan V. et al., 2019, MNRAS, 487, 444
Rembold S. B. et al., 2017, MNRAS, 472, 4382
Rich J. A., Kewley L. J., Dopita M. A., 2011, ApJ, 784, 87
Rich J. A., Kewley L. J., Dopita M. A., 2014, ApJ, 781, L12
Rich J. A., Kewley L. J., Dopita M. A., 2015, ApJS, 221, 28
Richings A. J., Faucher-Gière C.-A., 2018a, MNRAS, 474, 3663
Richings A. J., Faucher-Gière C.-A., 2018b, MNRAS, 478, 3100
Riffel R. A., Sorchi-Bergmann T., Winge C., Barbosa F. K. B., 2006, MNRAS, 373, 2
Riffel R. A., Storchi-Bergmann T., Winge C., McGregor P. J., Beck T., Schmitt H., 2008, MNRAS, 385, 1129
Riffel R. A., Sorchi-Bergmann T., Dors O. L., Winge C., 2009, MNRAS, 393, 783
Riffel R. A., Storchi-Bergmann T., Winge C., 2013, MNRAS, 430, 2249
Riffel R. A., Storchi-Bergmann T., Riffel R., 2015, MNRAS, 451, 3587
Riffel R. A. et al., 2019, MNRAS, 485, 5590
Rigopoulou D., Kunze D., Lutz D., Genzel R., Moorwood A. F. M., 2002, A&A, 389, 374
Roussel H. et al., 2007, ApJ, 669, 959
Sales D. A., Pastoriza M. G., Riffel R., 2010, ApJ, 725, 605
Sarzi M. et al., 2006, MNRAS, 366, 1151
Scannapieco E., Brüggen M., 2015, ApJ, 805, 158
Schnorr-Müller A., Storchi-Bergmann T., Nagar N. M., Robinson, A. Lena D., Riffel R. A., Couto G. S., 2014, MNRAS, 437, 1708
Schönell A. J., Storchi-Bergmann T., Riffel R. A., Riffel R., Bianchin M., Dahmer-Hahn L. G., Diniz M. R., Dametto N. Z., 2019, MNRAS, 485, 2054
Shimizu T. T. et al., 2019, MNRAS, 490, 5860
Slater R. et al., 2019, A&A, 621, A83
Soto-Pinto P. et al., 2019, MNRAS, 489, 4111
Stierwalt S. et al., 2014, ApJ, 790, 124
Storchi-Bergmann T., Schnorr-Müller A., 2019, Nat. Astron., 3, 48
Storchi-Bergmann T., Simões Lopes R., McGregor P. , Riffel R. A., Beck T., Martini P., 2010, MNRAS, 402, 819
Terlevich R., Melnick J., 1985, MNRAS, 213, 841
Thomas D. et al., 2013, MNRAS, 431, 1383
Veilleux S. et al., 2013, ApJ, 776, 27
Whittle M., 1985, MNRAS, 216, 817
Woo J.-H., Son D., Bae H.-J., 2017, ApJ, 839, 120
Wright E. L. et al., 2010, AJ, 140, 1868
Yu X. et al., 2019, MNRAS, 486, 4463

Zakamska N. L., 2010, Nature, 465, 60

Zakamska N. L., Strauss M. A., Heckman T. M., Ivezić Ž., Krolik J. H., 2004, AJ, 128, 1002

Zakamska N. L. et al., 2016a, MNRAS, 455, 4191

Zakamska N. L. et al., 2016b, MNRAS, 459, 3144

Zhang D., Thompson T. A., Quataert E., Murray N., 2017, MNRAS, 468, 4801

This paper has been typeset from a T$_{\rm E}$X/L$^{\rm A}$T$_{\rm E}$X file prepared by the author.